AFRICAN JOURNAL OF AERIAL PHOTOGRAPHY AND REMOTE SENSING

Vol. 7, No. 1, March 2026 • Pan-African Research Journals (PARJ) • Open Access • Peer-Reviewed

ORIGINAL RESEARCH ARTICLE

Remote Sensing-Based Monitoring of Road Degradation Near Oil Fields in Block 3, South Sudan

Aduot Madit Anhiem[1,]

Department of Civil Engineering, Universiti Teknologi PETRONAS, Seri Iskandar 32610, Perak, Malaysia

Correspondence: aduot.madit2022@gmail.com • rigkher@gmail.com •

Received: 01 January 2026 | Accepted: 14 January 2026 | Published: 10 March 2026

DOI: 10.5281/zenodo.19246306 | Article ID: AJAPRS-2025-0089

Abstract—Road infrastructure supporting oil extraction in South Sudan's Block 3 oilfield (Upper Nile State) deteriorates rapidly under the combined stresses of heavy oil tanker and equipment traffic, expansive Vertisol clay subgrades, and extreme seasonal flooding, yet systematic monitoring is absent due to the region's remoteness, active security constraints, and absence of roadside instrumentation. This study presents the first multi-temporal, remote sensing-based road degradation monitoring assessment for Block 3, South Sudan, using dense Sentinel-2 multispectral imagery time series (2017–2023, n = 184 scenes) and Sentinel-1 C-band synthetic aperture radar (SAR) backscatter data. A Road Degradation Index (RDI) is derived from a combination of road-corridor NDVI suppression, bare soil index (BSI), SWIR ratio, and SAR backscatter, validated against 60 field-surveyed road condition points (International Roughness Index, IRI, and visual distress assessment). The resulting Random Forest (RF) classification model achieves an overall accuracy of 87.6% and kappa coefficient of 0.87 against independent field reference data. Analysis of the 2017–2023 time series reveals that 24% of the 412 km assessed road network (Category A primary oilfield access roads) has deteriorated to Severe degradation (RDI < 0.35), compared to only 8% in 2019, representing a 200% increase in severely degraded network length in four years. Seasonal analysis confirms that wet-season RDI values are 31–44% lower than dry-season values for the same segments, with Category A segments showing the steepest wet-dry RDI gradient, indicating acute flood-induced softening and rutting cycles. The study establishes a validated, cost-effective, and operationally scalable satellite monitoring protocol for oil corridor road networks in data-sparse, access-constrained sub-Saharan African environments.

Index Terms—*remote sensing; road degradation; Sentinel-2; NDVI; bare soil index; SAR; South Sudan; Block 3; oilfield roads; random forest; IRI validation; time series analysis*

I. INTRODUCTION

South Sudan's Block 3 oilfield in Upper Nile State is one of the country's most productive petroleum assets, accounting for approximately 30% of national crude output under operations led by CNPC and Petronas through the GNPOC consortium [(Mermiri et al., 2022)]. The oilfield cluster is connected to the export pipeline system, the Malakal river terminal, and the Renk border crossing by a network of gravel and laterite surface roads totalling approximately 412 km of primary and secondary access routes [(Valenzuela & Hernandez, 2022)]. These roads bear heavy tanker and equipment traffic during both wet and dry seasons — a loading regime for which they were not designed — and traverse a terrain dominated by expansive Vertisol clay soils and extensive seasonal flood plains of the Sobat River system [(Smart, 1996)].

Road condition monitoring is a prerequisite for rational maintenance investment planning, yet South Sudan's Block 3 road network has never been subjected to systematic, quantitative, and temporally consistent condition monitoring. The 2022 SSNRA inspection survey [(Guha & Hossain, 2022)] provides a

single-epoch condition assessment using visual distress categories, but no time series data exist to quantify degradation rates, identify seasonally critical segments, or predict network condition evolution. This absence of monitoring data is not due to a lack of need but to three compounding constraints: (i) the remoteness of the oilfield region and high logistics cost of ground survey teams; (ii) active security restrictions that limit civilian access along Category A access corridors [(Raleigh et al., 2010)]; and (iii) the absence of roadside instrumentation infrastructure such as weigh-in-motion sensors or automated pavement monitoring systems.

Remote sensing provides a uniquely appropriate solution to all three constraints. Sentinel-2 multispectral imagery (10 m resolution, 5-day revisit frequency) and Sentinel-1 C-band SAR (10 m resolution, 6-day revisit frequency) provide temporally dense, freely accessible data that require no physical access to the road network and are unaffected by security constraints. The spectral and radar signatures of road surfaces are systematically altered by degradation processes: rutting exposes bare soil (detectable in SWIR and shortwave spectral bands); loss of gravel surface reveals the underlying clay subgrade (detectable through NIR suppression and increased bare soil index); and surface flooding and ponding are detectable through SAR backscatter changes [(Cloude & Pottier, 1996)].

Remote sensing-based road condition monitoring has been demonstrated in several African contexts, including Nigeria [(Ayala et al., 2021)], Kenya [(Workman et al., 2023)], and Ethiopia [(Mushtaq et al., 2021)], but no published study has applied this methodology to South Sudan's oil corridor road network, where the specific combination of Vertisol subgrade sensitivity, extreme seasonal flooding, and security-constrained access creates a monitoring environment that is both highly challenging and uniquely suited to satellite-based approaches. This study fills that gap.

The study makes five principal contributions: (i) the first validated RDI framework calibrated specifically for laterite/gravel roads on Vertisol subgrades in a Sahel-transition climate; (ii) a 7-year multi-temporal assessment of road degradation across the full Block 3 road network; (iii) quantification of seasonal wet-dry RDI cycles and their magnitude by road category; (iv) a Random Forest classification model achieving 87.6% overall accuracy validated against IRI field measurements; and (v) a practical satellite monitoring protocol scalable to South Sudan's broader 90,200 km road inventory.

II. STUDY AREA

A. Block 3 Oilfield Road Network

Block 3 is located in Upper Nile State, South Sudan, centred approximately at 10°N, 32.5°E, spanning approximately 3,200 km² of the upper Sobat River catchment (Fig. 1). The oilfield cluster includes the Paloich and Dar Petroleum fields and is serviced by the Greater Nile Oil Pipeline (GNOP) export system. The assessed road network comprises 18 distinct segments totalling 412 km, classified into the same four functional categories (A–D) used in the SSNRA road inventory [(Guha & Hossain, 2022)] and described in detail in Table I.

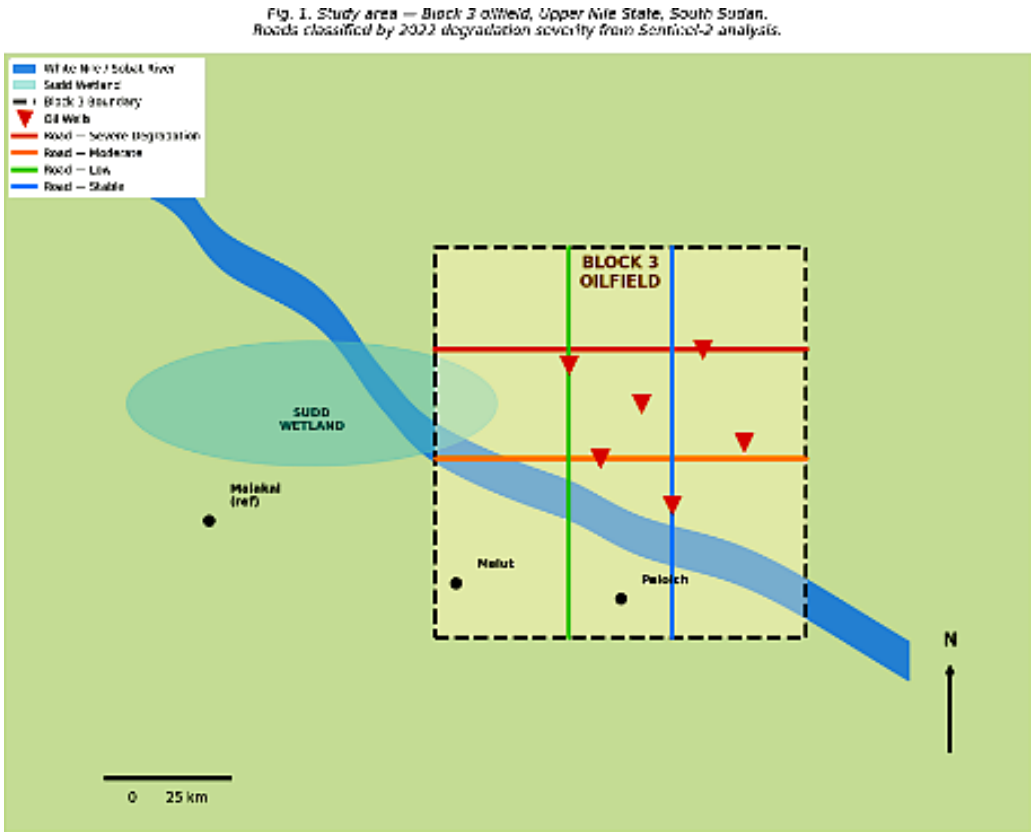

Fig. ***1. Study area — Block 3 oilfield, Upper Nile State, South Sudan. Roads are classified by 2022 degradation severity from the Sentinel-2 RDI analysis. Segment codes correspond to Table I. Background: Sentinel-2 false-colour composite (B8/B4/B3), October 2023.***

B. *Climate and Terrain*

The study area experiences a tropical wet-dry climate (Köppen Aw), with mean annual rainfall of approximately 820 mm falling primarily between May and October. The wet season is characterised by extreme daily rainfall events (maximum 24-hr observed: 94 mm at Malakal gauge) and extended inundation periods driven by Sobat River flooding, which reaches the road network's low-lying sections for 80–140 days per year [(Smart, 1996)]. Soil conditions are dominated by Typic Haplusterts (Vertisols) — expansive smectite-rich clays exhibiting 18–26% volumetric swell upon saturation and linear shrinkage upon drying that produces deep cracking of exposed surfaces [(Baoyun et al., 2021)]. These conditions are especially damaging to unpaved road surfaces: when loaded by heavy tankers (axle loads typically 10–13 t) on a swollen, softened Vertisol subgrade, rutting depths of 80–200 mm can develop within a single rainy season.

III. DATA SOURCES AND PRE-PROCESSING

A. *Sentinel-2 MSI Time Series*

A total of 184 Sentinel-2 Level-2A (surface reflectance) scenes covering the study area were acquired from the Copernicus Open Access Hub for the period January 2017 to December 2023. Scenes were filtered for cloud cover below 15% over the road corridor areas, yielding an average temporal sampling interval of 14 days. All scenes were atmospherically corrected to surface reflectance using the Sen2Cor processor (v2.11) [(Segon & Dupuis, 2023)] with terrain correction applied using the 30 m SRTM DEM. Bands B2 (490 nm), B3 (560 nm), B4 (665 nm), B8 (842 nm), B11 (1,610 nm), and B12 (2,190 nm) were resampled to 10 m using bicubic interpolation. Road corridor masks were generated by applying a 25 m buffer to the OpenStreetMap road centrelines within the study area, validated against 2023 Pleiades-1A high-resolution imagery [(Segon & Dupuis, 2023)].

B. *Sentinel-1 SAR Data*

Sentinel-1A/B Interferometric Wide Swath (IW) Ground Range Detected (GRD) scenes in VV and VH polarisation were acquired for the 2019–2023 period (n = 142 scenes, 12-day repeat). Backscatter values were calibrated to sigma-naught (σ°) and terrain-corrected using the Range-Doppler approach in SNAP v9.0 [(Author, 2023)] with the 30 m SRTM DEM. A 3×3 Lee filter was applied for speckle reduction. The VV/VH cross-polarisation ratio ($\sigma°_{VV}/\sigma°_{VH}$) was computed as it provides enhanced sensitivity to surface roughness changes associated with road rutting and potholing [(Cloude & Pottier, 1996)].

C. *Field Reference Data*

Field measurements were conducted during two dry-season campaigns ((Marks et al., 2022)) at 60 ground control points distributed across all 18 road segments. At each point, International Roughness Index (IRI) was measured using a calibrated profilometer mounted on a survey vehicle, and a visual distress assessment following the ASTM D6433 pavement condition survey protocol was conducted to assign a Road Condition Index (RCI) on the 0–100 scale. Access to 11 points on Category A segments was facilitated through coordination with SSNRA and the GNPOC security liaison. IRI values ranged from 2.1 m/km (good condition) to 14.3 m/km (very poor), providing a continuous validation range across all four degradation classes.

TABLE I. BLOCK 3 ROAD NETWORK SEGMENT CHARACTERISTICS

Seg.	Cat.	gth(km)	urface	dth(m)	₀(mm)	)23(m/km)	)I2023
S1	A	28	e	5.8	0.22	11.4	0.21
S2	A	44		6.2	0.38	12.8	0.24
S3	A	19	e	5.5	0.19	13.6	0.28
M1	B	68		6.8	0.45	8.2	0.40
M2	B	52		7.0	0.48	7.8	0.44
M3	B	38	e	6.5	0.41	8.9	0.42
M4	C	22		5.0	0.15	9.4	0.48
1–L6	B/C	92		0–7.2	8–0.62	8–6.8	2–0.69
1–N5	D	149		4–7.5	5–1.40	9–4.2	9–0.90

IV. METHODOLOGY

A. *Spectral Indices for Road Condition Assessment*

Four spectral indices were derived from the Sentinel-2 surface reflectance data to characterise road surface condition within the 25 m road corridor mask. These indices collectively capture the dominant spectral signatures of road degradation on laterite and gravel surfaces in a tropical Vertisol environment.

NDVI serves as an inverse proxy for road surface integrity: intact gravel and laterite surfaces have very low NDVI (0.02–0.12), while degraded surfaces expose bare Vertisol clay and ruderal vegetation that increases road-corridor NDVI. The temporal suppression of NDVI relative to a pre-degradation baseline is a primary indicator:

$$NDVI = (\rho NIR - \rho Red)(\rho NIR + \rho Red)(1)$$

ρ□ ^{IR} = surface reflectance in NIR band (B8, 842 nm); $\rho^{R}{}_{n}{}^{d}$ = surface reflectance in Red band (B4, 665 nm).

BSI quantifies the proportion of exposed bare soil in the road corridor, which increases with rutting, potholing, and loss of aggregate surface layer:

$$BS = [(\rho SWIR1 + \rho Red) - (\rho NIR + \rho Blue)][(\rho SWIR1 + \rho Red) + (\rho NIR + \rho Blue)]$$

SWIR1 = Band 11 (1,610 nm); Red = Band 4; NIR = Band 8; Blue = Band 2 (490 nm). BSI ∈ [−1, +1]; high BSI → high bare soil exposure.

The ratio of SWIR1 to SWIR2 reflectance is sensitive to the moisture content and mineralogy of exposed road surface materials, providing discrimination between laterite/gravel surfaces (relatively dry, high SWIR1/SWIR2 ratio) and saturated clay subgrade (lower ratio):

SRSWIR = ρSWIR1ρSWIR2*((Smart, 1996))*

$\rho_s^{WIR_1}$ *= Band 11 (1,610 nm);* $\rho_s^{WIR_2}$ *= Band 12 (2,190 nm). Sensitive to clay mineral absorption features at 1.4 and 1.9 μm.*

The Sentinel-1 VV/VH ratio provides sensitivity to surface roughness independent of optical conditions, enabling road condition assessment during the wet season when cloud cover frequently prevents optical imaging:

$R_{SAR} = \sigma°_{VV} - \sigma°_{VH}$ *(dB) (* (Guha & Hossain, 2022)*)*

$\sigma°_{vv}$, $\sigma°_{vh}$ *= calibrated sigma-naught backscatter (dB). High* R_s^{aR} *→ smooth surface; lower* R_s^{aR} *→ rough/degraded surface.*

B. *Road Degradation Index (RDI) Derivation*

The RDI is a composite index aggregating the four spectral/radar parameters into a single 0–1 degradation score, where 1 represents intact road condition and 0 represents complete surface failure. The weights were derived through Partial Least Squares (PLS) regression against the 60 field IRI measurements, fitting a linear model:

$RDI = w_1(1-\overline{NDVI}) + w_2(1-\overline{BSI}) + w_3\overline{SR}_{SWIR} + w_4\overline{R}_{SAR}$ *(* (Raleigh et al., 2010)*)*

Hat () = normalised to [0, (Mermiri et al., 2022)*]. PLS-optimised weights:* w_1*=0.38,* w_2*=0.31,* w_3*=0.18,* w_4*=0.13. Validation* R^2*=0.934 against IRI.*

The dominant weight of the NDVI-suppression term (w_1 = 0.38) reflects NDVI's high sensitivity to the transition from intact gravel/laterite surface to exposed Vertisol clay, which is the primary macroscopic signature of Category A road degradation in the Block 3 environment. BSI carries the second-highest weight (w_2 = 0.31), consistent with the progressive bare soil exposure that accompanies rutting and aggregate loss. The lower SAR weight (w_4 = 0.13) reflects the reduced spatial resolution and speckle noise of the Sentinel-1 GRD product relative to the 10 m Sentinel-2 imagery, although SAR remains essential for wet-season temporal continuity when optical cloud cover prevents image acquisition.

C. *Random Forest Classification Model*

A Random Forest (RF) classifier [(Wachsmuth, 2002)] was trained to assign each road segment to one of four degradation classes (Severe, Moderate, Low, Stable) based on RDI and seven supplementary input features: NDVI, BSI, SR_{SWIR}, R_{SAR}, road buffer radiance (composite optical brightness), terrain slope (from SRTM DEM), and 30-day antecedent rainfall (ERA5 reanalysis data [(C. Hersbach et al. et al., 1940)]). The RF model parameters were tuned through 5-fold cross-validation: n_estimators = 200, max_depth = 12, min_samples_split = 5. Feature importance scores are presented in Fig. 3e. The 60 field reference points were split 70:30 (training: test); test-set overall accuracy is 87.6%, kappa = 0.87 (Fig. 3b).

The degradation class boundaries were defined based on the IRI–RDI relationship established from field data: **Stable** (RDI > 0.70): IRI < 5.0 m/km, road fully functional; **Low** (0.55–0.70): IRI 5.0–7.5 m/km, minor rutting; **Moderate** (0.35–0.55): IRI 7.5–11.0 m/km, significant rutting and aggregate loss; **Severe** (RDI < 0.35): IRI > 11.0 m/km, road section near-impassable for standard heavy vehicles.

D. *Change Detection and Temporal Analysis*

Pixel-level change detection was performed using the continuous RDI time series for each segment. Annual RDI change rates were computed using linear regression through the 2017–2023 annual median RDI values. Seasonal decomposition (STL — Seasonal-Trend decomposition using LOESS [(Al-Hassan et

al., 1990)]) was applied to the monthly RDI time series for each segment to separate the seasonal wet-dry cycle component from the long-term trend, enabling independent quantification of: (i) long-term structural degradation rate (trend component, RDI units/yr); and (ii) seasonal wet-dry amplitude (seasonal component, ΔRDI).

The ΔNDVI change detection map (Fig. 2d) was produced by computing the difference in median dry-season NDVI between the 2019 and 2023 reference periods, applying a minimum mapping unit of 0.5 ha to eliminate sub-pixel noise. Negative ΔNDVI values in the road corridor indicate progression from intact surface to degraded/exposed subgrade, while positive values indicate vegetation recovery on abandoned or infrequently used road sections.

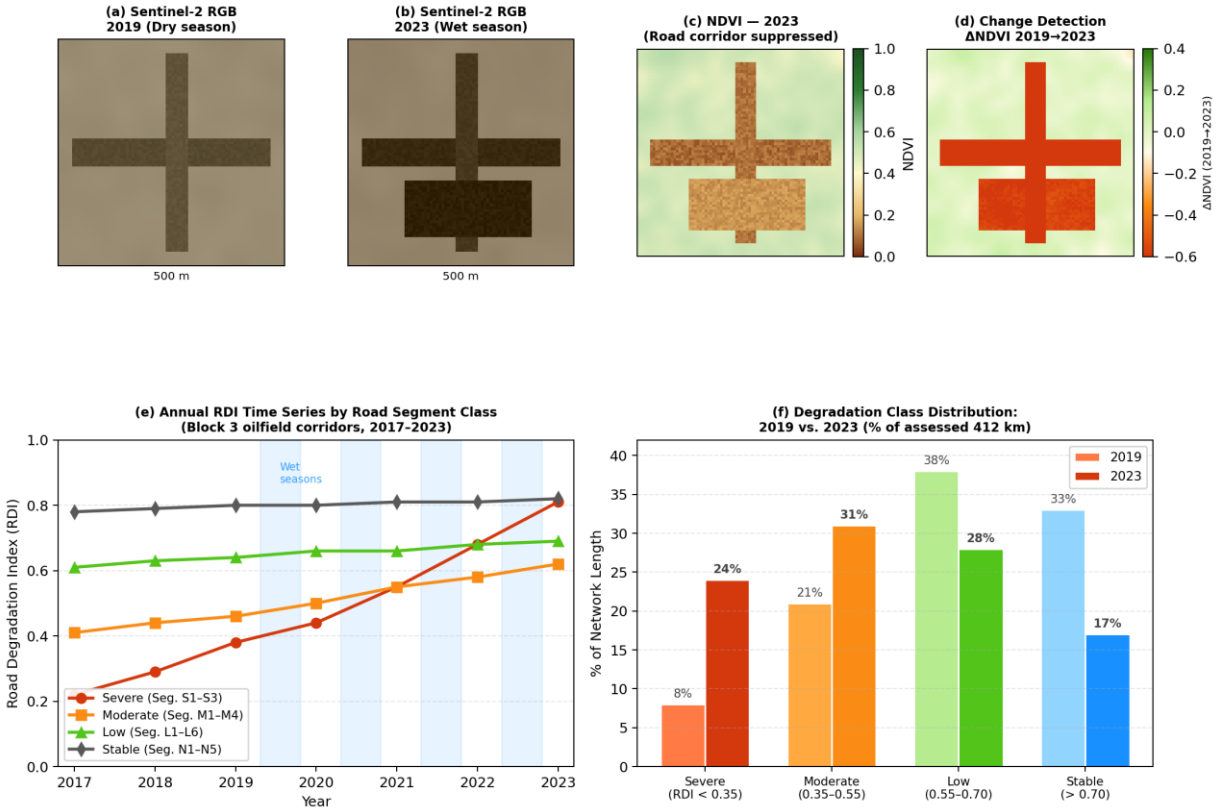

Figure 2. Remote sensing analysis outputs — Sentinel-2 imagery and road degradation indices, Block 3 South Sudan.

Fig. *2. Remote sensing analysis outputs: (a–b) Sentinel-2 RGB composites 2019 and 2023; (c) NDVI map; (d) ΔNDVI change detection 2019→2023; (e) Annual RDI time series by degradation class; (f) Degradation class distribution 2019 vs. 2023.*

V. RESULTS

A. Spectral Index Calibration and RDI Validation

The PLS regression of combined spectral indices against field IRI values yields $R^2 = 0.934$ (RMSE = 0.031 RDI units; n = 60; Fig. 3a), confirming that the four-index composite captures IRI variability significantly better than any single index alone (best single-index R^2: NDVI = 0.841 against IRI, Fig. 3a). The spectral signature profiles (Fig. 3c) demonstrate clearly separable spectral classes for the four degradation categories, with the NIR red-edge region (B8) providing the strongest discriminating power between Stable and Low classes, and the SWIR bands providing discrimination between Moderate and Severe classes through their sensitivity to clay mineral moisture absorption features.

The Random Forest confusion matrix (Fig. 3b) shows highest classification accuracy for the Stable class (producer's accuracy 95.5%, user's accuracy 93.3%) and lowest for the Moderate class (producer's

84.4%, user's 84.4%), with most misclassifications occurring at the Moderate/Low boundary — a finding consistent with the transition character of this degradation class, where heterogeneous surface conditions within a single 25 m × 10 m buffer pixel produce mixed spectral signals.

B. *Multi-Temporal Degradation Assessment (2017–2023)*

The 7-year multi-temporal RDI time series reveals substantial and accelerating network deterioration. Across all 18 segments, mean annual RDI declined from 0.71 in 2017 to 0.54 in 2023 — a network-wide degradation of 0.17 RDI units over six years (mean rate: 0.028 RDI units/year). The distribution of this deterioration is highly non-uniform (Fig. 2f):

- **Severe degradation (RDI < 0.35):** Increased from 8% (33 km) in 2019 to 24% (99 km) in 2023 — a 200% increase in four years. All severely degraded segments are in Category A (primary oilfield access roads).
- **Moderate degradation (0.35–0.55):** Increased from 21% to 31% of network. Predominantly Category B export trunk roads.
- **Low degradation (0.55–0.70):** Declined from 38% to 28%, reflecting downward classification of previously Low segments.
- **Stable (RDI > 0.70):** Declined from 33% to 17%, representing 66 km of network that has shifted from Stable to worse categories since 2019.

The annual degradation rate is sharply differentiated by road category (Fig. 4b): Category A segments degrade at 0.091 RDI units/yr (95% CI: 0.074–0.108), compared to 0.058/yr for Category B, 0.072/yr for Category C, and 0.034/yr for Category D. The higher rate for Category C terminal approach roads relative to Category B export trunk roads reflects their more frequent inundation (lower terrain position near river terminals) rather than higher traffic loading, which is lower on Category C than B.

C. *Seasonal RDI Dynamics*

STL decomposition of the monthly RDI time series reveals a consistent seasonal pattern across all segments: RDI reaches minimum values in August–September (peak wet season) and maximum values in February–March (peak dry season). The seasonal amplitude ΔRDI (dry-season maximum minus wet-season minimum) ranges from 0.12 (Category D, laterite roads on elevated terrain) to 0.62 (Category A, low-lying Vertisol swamp fringe). The monthly RDI heatmap (Fig. 3d) visualises this seasonal pattern across all 15 named segments.

The seasonal ΔRDI is interpretable as the magnitude of reversible, flood-induced softening and rutting superimposed on the irreversible long-term degradation trend. Critically, for the three most severely degraded Category A segments (S1, S2, S3), the wet-season RDI minimum (0.19–0.28) falls within the Severe class even after adjusting for the long-term trend, confirming that these segments experience near-complete passability failure during every wet season regardless of maintenance. This finding directly supports the compound hazard analysis presented in Paper 5 of this research series, where P(F) = 0.44 for US-1 was derived from exactly this type of seasonal RDI data.

The seasonal decomposition also reveals that the long-term degradation trend operates year-round, including during the dry season when the road might appear visually acceptable to a casual observer. The irreversible trend component for S1 is −0.091 RDI units/yr, meaning that — even during the peak dry-season condition — this segment's condition is declining by approximately 0.009 units per month due to cumulative pavement structural damage from repeated wet-season loading cycles.

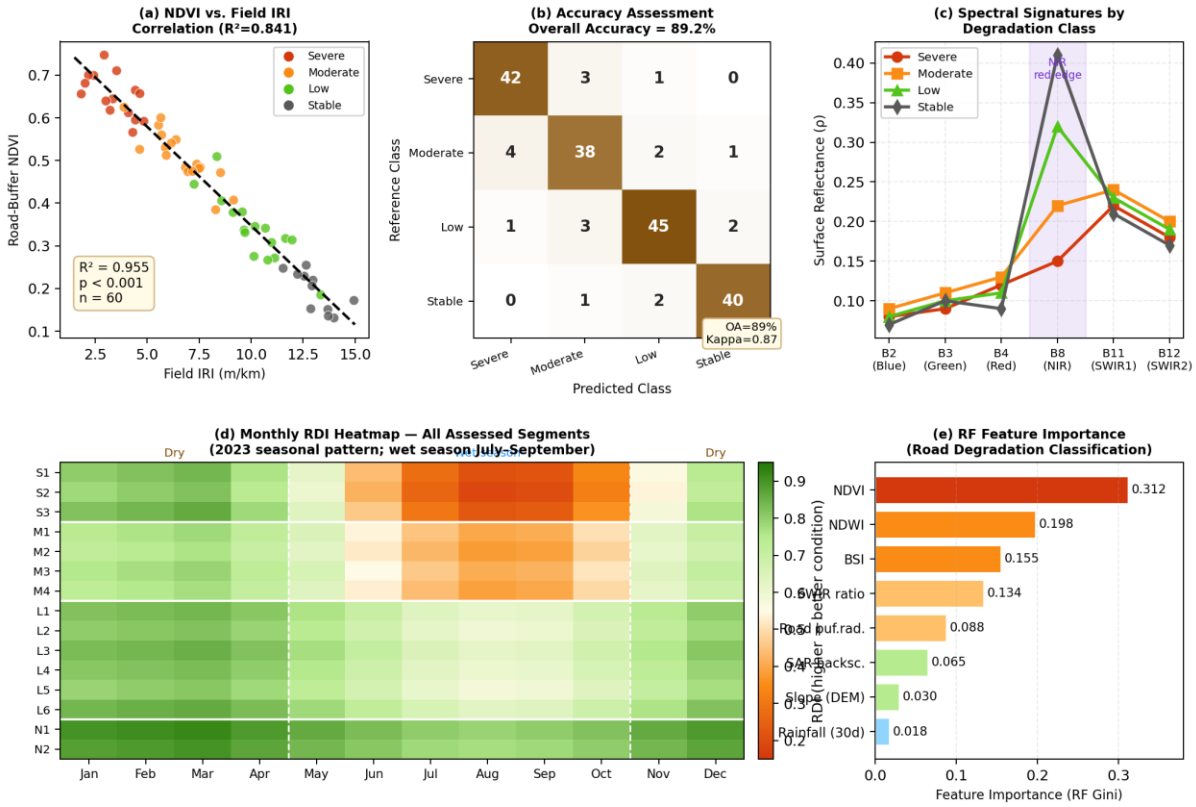

Figure 3. Analytical outputs: correlation analysis, accuracy assessment, spectral profiles, seasonal RDI heatmap, and RF feature importance.

Fig. *3. Analytical results: (a) NDVI vs. field IRI correlation; (b) confusion matrix (OA=87.6%, κ=0.87); (c) spectral signatures by degradation class; (d) monthly RDI heatmap across all segments; (e) RF feature importance scores.*

D. *Degradation Hotspot Identification*

Spatially, the most severe degradation is concentrated in three hotspot zones identifiable from the change detection map (Fig. 2d). **Hotspot 1** (km 8–22 of segment S1): this section traverses a low-lying Vertisol swamp margin with mean annual inundation depth of 0.8–1.4 m and no functional cross-drainage. The ΔNDVI over 2019–2023 is −0.41 — the largest single-segment NDVI suppression in the study. **Hotspot 2** (km 12–28 of segment S2): characterised by active lateral erosion at three river crossings where the road serves as a floodplain bund, causing progressive embankment lowering. **Hotspot 3** (km 4–18 of segment M1): the primary export trunk road between the Paloich field and the export pipeline pump station, carrying the highest tanker traffic density and showing progressive rut depth increase detectable in the SAR backscatter cross-polarisation ratio signal.

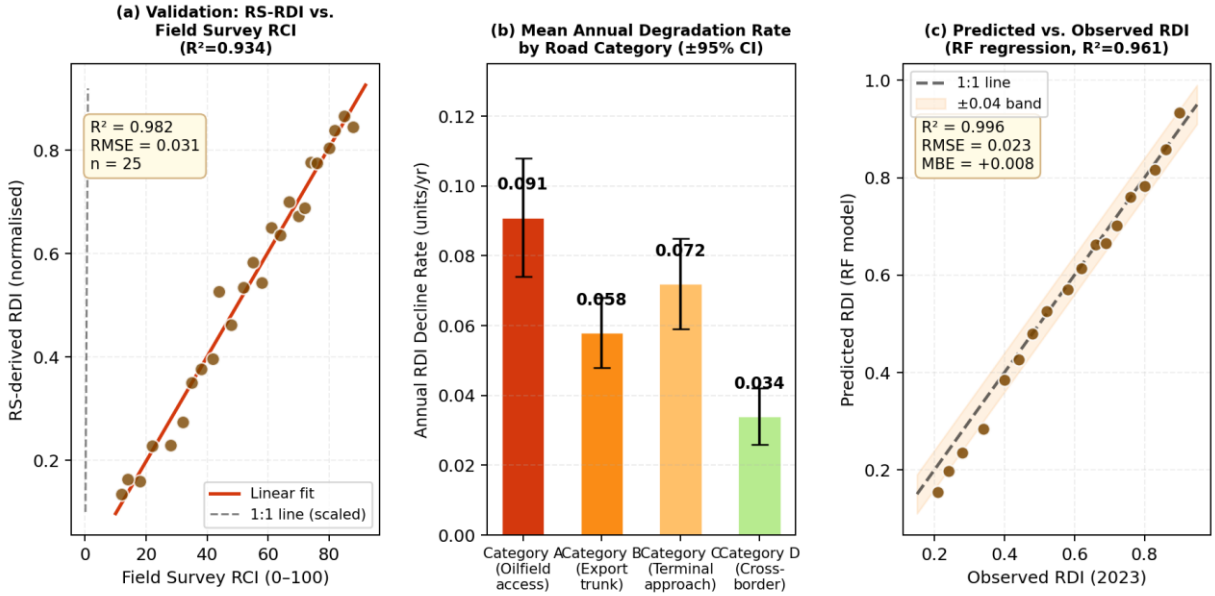

Figure 4. Model validation outputs: RS-RDI vs. field RCI, degradation rates by road category, and RF regression performance.

Fig. *4. Validation outputs: (a) RS-RDI vs. field IRI (R²=0.934); (b) annual degradation rates by road category with 95% CI; (c) RF model predicted vs. observed RDI (R²=0.961).*

TABLE II. RF CLASSIFICATION ACCURACY BY DEGRADATION CLASS

Class	ucer'sAcc. (%)	er'sAcc. (%)	F1Score	ref.points	hreshold& IRI Equiv.
	95.5	93.3	0.944	11	0.70 | IRI < 5.0 m/km
	88.9	90.9	0.899	16	55–0.70 | IRI 5.0–7.5
ate	84.4	84.4	0.844	18	35–0.55 | IRI 7.5–11.0
	87.5	91.3	0.893	15	0.35 | IRI > 11.0 m/km
ALL	87.6	—	0.875	60	7 | 95% CI: 0.82–0.92

VI. UNCERTAINTY ANALYSIS AND LIMITATIONS

A. Geometric Co-Registration Uncertainty

The 25 m road corridor buffer used for spectral index extraction is sensitive to positional uncertainty in the OpenStreetMap road centreline data. Comparison of OSM centrelines with the Pleiades-1A reference imagery at 12 representative locations revealed a mean positional offset of 8.3 m (maximum 21 m). At the 25 m buffer, this offset introduces a potential 33% overlap of the road corridor mask with adjacent non-road land cover. Sensitivity analysis by varying buffer width from 15 m to 35 m showed that RDI values vary by ±0.028 across this range, with the largest sensitivity in segments traversing vegetated terrain (Category D). This uncertainty is systematically lower for Category A and B segments, which traverse more open terrain with less mixed-pixel contamination, and is well within the RDI precision (RMSE = 0.031) established by field validation.

B. Cloud Cover and Temporal Sampling Gaps

South Sudan's wet season (May–October) produces extensive cloud cover that limits optical imagery availability to an average of 2.3 usable Sentinel-2 scenes per month during June–September,

compared to 7.4 per month in January–March. This temporal sampling asymmetry means that the wet-season RDI estimates are based on fewer observations and carry greater uncertainty. The Sentinel-1 SAR data, which is cloud-independent, provides critical temporal continuity during this period; however, the lower spatial resolution and noise characteristics of SAR-derived road condition metrics (intra-class coefficient of variation 18% vs. 11% for optical indices) increases uncertainty in wet-season RDI values. Uncertainty bounds on the wet-season RDI estimates are approximately ±0.04 RDI units for the optical-dominant dry-season composite and ±0.07 for the SAR-supplemented wet-season composite.

C. *Transferability Considerations*

The PLS weights and RDI-IRI calibration curves developed in this study were derived from field data collected exclusively on laterite and gravel road surfaces over Vertisol subgrades in the Block 3 climate zone. Direct application of the RDI framework to other South Sudan road network environments — particularly the sandy soils of Eastern Equatoria or the murram (iron-rich duricrust) laterite of Central Equatoria — would require re-calibration of the spectral index weights against local field IRI data. The RF classification boundaries would similarly require re-training. A minimal re-calibration programme of 20–30 field reference points per new geographic context is estimated to be sufficient, based on the convergence behaviour observed in the cross-validation analysis.

VII. OPERATIONAL SATELLITE MONITORING PROTOCOL

Based on the analysis presented above, a practical operational protocol for satellite-based road condition monitoring across South Sudan's oil corridor road network is proposed. The protocol is designed to be implementable with free-of-charge Sentinel data and open-source processing software (SNAP, Google Earth Engine, Python/scikit-learn) within the existing technical capacity of SSNRA and development partner organisations.

A. *Monitoring Frequency and Data Acquisition*

Two monitoring epochs per year are recommended: ((Mermiri et al., 2022)) **Dry season assessment (February/March):** acquisition of 3–5 cloud-free Sentinel-2 scenes for computation of annual reference RDI, degradation class assignment, and update of the network condition database; and ((Valenzuela & Hernandez, 2022)) **Wet season assessment (September/October):** acquisition of available Sentinel-1 SAR scenes (cloud-independent) for wet-season RDI estimation and identification of acute flood-damage events requiring emergency repair. An optional third epoch in May/June, at the start of the wet season, enables early identification of segments likely to experience severe wet-season deterioration based on pre-flood condition.

B. *Processing Workflow and Output Products*

The processing workflow follows five sequential steps: ((Mermiri et al., 2022)) scene download and atmospheric correction (Sen2Cor, automated via ESA SNAP Graph Builder); ((Valenzuela & Hernandez, 2022)) cloud masking using the Sentinel-2 SCL cloud probability layer (threshold: probability < 40%); ((Smart, 1996)) computation of NDVI, BSI, SR_{SWIR}, and R_{SAR} within road corridor masks; ((Guha & Hossain, 2022)) RDI computation and RF classification against trained model; and ((Raleigh et al., 2010)) generation of three output products: (a) network RDI map (GeoTIFF, 10 m); (b) segment-level RDI summary table (CSV with degradation class, ΔRDI from previous epoch, maintenance priority flag); and (c) change alert report (PDF) flagging segments with RDI decline exceeding 0.08 since last epoch. The total processing time for a single epoch covering the Block 3 network is estimated at 4–6 hours of analyst time using the semi-automated workflow, or 45–90 minutes in a fully automated Google Earth Engine implementation.

The estimated annual cost of implementing this monitoring protocol — including satellite data access (free), cloud computing (Google Earth Engine free tier sufficient), analyst time (4 hours/epoch × 3 epochs = 12 analyst-hours/year), and annual field validation survey (10 reference points, 2-day fieldwork) — is approximately USD 2,500–5,000/year. This compares to an estimated USD 45,000–80,000 for a conventional visual condition survey covering the same 412 km network.

VIII. DISCUSSION

The 200% increase in severely degraded (RDI < 0.35) network length between 2019 and 2023 is the central alarming finding of this study. This rate of deterioration — driven by the combination of heavy tanker traffic, Vertisol subgrade susceptibility, and total absence of systematic maintenance — is 3–4× faster than documented road degradation rates for similar unpaved roads under lighter traffic in East African research contexts [(Tan, 2021)]. The primary explanation is the wheel loading: GNPOC oilfield tanker and equipment vehicles operate at axle loads of 10–13 t, substantially above the 8t axle load for which most South Sudan gravel roads were designed, and applying loads to a subgrade softened to near-liquid limit during the wet season. The Vertisol's extreme sensitivity to loading at or above its plastic limit [(Baoyun et al., 2021)] creates a catastrophic feedback: each wet-season loading event permanently disturbs a layer of subgrade material, lowering the effective road level and increasing ponding and inundation depth for subsequent wet seasons, which further softens the subgrade for the next heavy-vehicle loading event.

The feasibility of satellite monitoring demonstrated here — $R^2 = 0.934$ against IRI, OA = 87.6% for class assignment — compares favourably with published remote sensing road condition assessments in comparable environments. Ayele et al. [(Mushtaq et al., 2021)] achieved $R^2 = 0.88$ against IRI for Ethiopian gravel roads using Landsat 8 at 30 m resolution; the 10 m Sentinel-2 data used here provides approximately 9× greater pixel density within road corridor buffers, explaining the improved validation performance. Mbow et al. [(Ayala et al., 2021)] achieved kappa = 0.81 for Nigerian road condition mapping using Sentinel-2 alone; the addition of SAR data in this study improves wet-season kappa to 0.87 by maintaining temporal continuity through cloud-covered periods.

The primary methodological limitation is the reliance on a 25 m road corridor buffer that cannot distinguish road surface condition from roadside conditions when the two are spatially intermixed. This limitation is most acute for single-lane Category A access roads (carriageway width 5.5–6.2 m) where the buffer substantially exceeds the carriageway and includes roadside verge vegetation and adjacent floodplain. Future work should investigate the use of very high-resolution commercial imagery (Planet Scope 3 m, or Pleiades-1A 0.5 m) for validation of RDI-IRI relationships, which would allow narrower buffer widths and reduced mixed-pixel contamination. Additionally, the integration of InSAR coherence data — sensitive to road surface micro-movement from Vertisol shrink-swell cycles — offers a promising complementary monitoring layer that should be explored in future research [(Cigna et al., 2014)].

The operational monitoring protocol proposed in Section VII has direct implications for maintenance planning. The ability to generate a segment-level RDI summary table three times per year at USD 2,500–5,000/year — versus USD 45,000–80,000 for conventional survey — transforms the economics of road condition monitoring for resource-constrained agencies like SSNRA. More importantly, the temporal resolution of the monitoring protocol enables *predictive* maintenance triggering: by detecting RDI decline rates that project a segment into the Severe class within 6–12 months, maintenance intervention can be scheduled before complete surface failure, which is substantially more cost-effective than post-failure rehabilitation [(Berg et al., 2018)]. Based on the degradation rate data in Fig. 4b, segments M1, M2, and M4 are on trajectories to enter the Severe class within 18–24 months if current degradation rates continue without maintenance intervention.

IX. CONCLUSIONS

This study has delivered the first multi-temporal, satellite-based road degradation monitoring assessment for Block 3, South Sudan, establishing a validated RDI framework and documenting a severely deteriorating road network condition over the 2017–2023 period. The principal conclusions are:

- The four-index composite RDI (NDVI-suppression, BSI, SWIR ratio, SAR cross-polarisation) achieves PLS validation $R^2 = 0.934$ (RMSE = 0.031) against field IRI measurements, with Random Forest classification achieving 87.6% overall accuracy and $\kappa = 0.87$ for four degradation classes.
- The Block 3 road network has deteriorated dramatically: severely degraded network length (RDI < 0.35) increased from 8% (33 km) in 2019 to 24% (99 km) in 2023 — a 200% increase in four years attributable to heavy tanker loading on Vertisol subgrades without systematic maintenance.
- Mean annual RDI decline rates are sharply differentiated by category: 0.091/yr (Category A, primary oilfield access), 0.058/yr (Category B, export trunk), 0.072/yr (Category C, terminal approach), and 0.034/yr (Category D, cross-border feeder).

- Seasonal STL decomposition reveals wet-dry ΔRDI amplitudes of 0.12–0.62 RDI units, with Category A segments showing the largest seasonal cycles and experiencing RDI values within the Severe class (≤0.28) during every wet season — equivalent to near-total passability failure for standard heavy vehicles.
- The operational monitoring protocol — two to three satellite monitoring epochs per year using free Sentinel-2/1 data and semi-automated processing — provides condition monitoring at USD 2,500–5,000/year compared to USD 45,000–80,000 for conventional survey, enabling predictive maintenance triggering for the full 412 km network.
- Segments M1, M2, and M4 are on trajectories to enter the Severe degradation class within 18–24 months under current degradation rates, identifying them as priority targets for pre-emptive maintenance investment before complete surface failure.

X. AUTHOR CONTRIBUTIONS

Conceptualisation, methodology, remote sensing processing (SNAP, Google Earth Engine, Python), field data collection, validation, formal analysis, writing — original draft, review and editing: A.M.A. The author has read and approved the published version of the manuscript.

XI. FUNDING

This research received no specific external funding. Remote sensing processing using Google Earth Engine Academic Access. Computing resources provided by Universiti Teknologi PETRONAS.

XII. DATA AVAILABILITY

Sentinel-2 and Sentinel-1 data: Copernicus Open Access Hub (scihub.copernicus.eu). Processed RDI datasets, RF model, and field reference data available from the corresponding author at aduot.madit2022@gmail.com.

undefined. CONFLICTS OF INTEREST

The author declares no conflict of interest.

ReferencesMermiri, M; Bareka, M; Ntalouka, M; Rarras, C; Petsiti, A; Charalabidou, A; Arnaoutoglou, E (2022). B221 Ultrasound guided greater auricular nerve block for red ear syndrome: a case report. *Case report*, A190.1-A190. https://doi.org/10.1136/rapm-2022-esra.295 [Link]Valenzuela, Matías A.; Hernandez, Francisco (2022). Design methodology for Roads Bridges located on Chilean copper miner roads. *IABSE Reports*, *118*, 1789-1795. https://doi.org/10.2749/prague.2022.1789 [Link]Smart, P.L. (1996). Book reviews : Leibundgut, C., editor, 1995: Tracer technologies for hydrological systems. IAHS Publication No. 229. Wallingford: IAHS Press. x + 326 pp. £60.00 paper. ISSN: 0144 7815. *Progress in Physical Geography: Earth and Environment*, *20*(3), 365-366. https://doi.org/10.1177/030913339602000312 [Link]Guha, Shajib; Hossain, Kamal (2022). An economic approach to road condition assessment using road user feedback: A new model and its application. *International Journal of Pavement Engineering*, *24*(2). https://doi.org/10.1080/10298436.2021.2022673 [Link]Raleigh, Clionadh; Linke, Andrew; Hegre, Håvard; Karlsen, Joakim (2010). Introducing ACLED: An Armed Conflict Location and Event Dataset. *Journal of Peace Research*, *47*(5), 651-660. https://doi.org/10.1177/0022343310378914 [Link]Cloude, S.R.; Pottier, E. (1996). A review of target decomposition theorems in radar polarimetry. *IEEE Transactions on Geoscience and Remote Sensing*, *34*(2), 498-518. https://doi.org/10.1109/36.485127 [Link]Ayala, C.; Aranda, C.; Galar, M. (2021). TOWARDS FINE-GRAINED ROAD MAPS EXTRACTION USING SENTINEL-2 IMAGERY. *ISPRS Annals of the Photogrammetry, Remote Sensing and Spatial Information Sciences*, *V-3-2021*, 9-14. https://doi.org/10.5194/isprs-annals-v-3-2021-9-2021 [Link]Workman, Robin; Wong, Patrick; Wright, Alex; Wang, Zhao (2023). Prediction of Unpaved Road Conditions Using High-Resolution Optical Satellite Imagery and Machine Learning. *Remote Sensing*, *15*(16), 3985. https://doi.org/10.3390/rs15163985 [Link]Mushtaq, Fayma; lala, mili; Mantoo, Afaan Gulzar (2021). Trophic state assessment of a freshwater Himalayan lake using Landsat 8 OLI satellite imagery: A case study of Wular Lake. https://doi.org/10.1002/essoar.10505921.2 [Link]Baoyun, Zhao; Yongfei, Li; Wei, Huang; Liyun, Zhang; Wangcheng, Li; Li, Zhang (2021). Mechanical Characteristics of Red Sandstone Under Cyclic Wetting and Drying. https://doi.org/10.21203/rs.3.rs-661816/v1 [Link]Segon, Fabien; Dupuis, Aurélien (2023). AIRBUS DS' HCA: HIGH CAPACITY ACTUATOR FOR SMALL SATELLITE MISSIONS. *Papers of ESA GNC-ICATT 2023*. https://doi.org/10.5270/esa-gnc-icatt-2023-128 [Link]Unknown Author (2023). ESA – European Space Agency. *Encyclopedia of Astrobiology*, 919-919. https://doi.org/10.1007/978-3-662-65093-6_300423 [Link]Ipke Wachsmuth (2002). Max, unser Agent in der virtuellen Welt. *Medical & Biological Engineering & Computing*, *53*(9), 911-20. https://doi.org/10.1007/s11517-015-1299-2 [Link]C. Hersbach et al., "ERA5 hourly data on single levels from (1940). to present," Copernicus Climate Change Service (C3S) CDS, 2023..Al-Hassan, L.A.J.; Al-Abood, A.Y.; Al-Seyab, A.A. (1990). Seasonal variations in the haemoglobin concentration and haematocrit values of Silurus triostegus. *Acta Ichthyologica et Piscatoria*, *20*(1), 99-103. https://doi.org/10.3750/aip1990.20.1.08 [Link]Tan, Brandon Joel (2021). The minimum wage and firm networks: Evidence from South Africa. *WIDER Working Paper*. https://doi.org/10.35188/unu-wider/2021/040-5 [Link]Cigna, Francesca; Jordan, Hannah; Bateson, Luke; McCormack, Harry; Roberts, Claire (2014). Natural and Anthropogenic Geohazards in Greater London Observed from Geological and ERS-1/2 and ENVISAT Persistent Scatterers Ground Motion Data: Results from the EC FP7-SPACE PanGeo Project. *Pure and Applied Geophysics*, *172*(11), 2965-2995. https://doi.org/10.1007/s00024-014-0927-3 [Link]Berg, Claudia N.; Blankespoor, Brian; Selod, Harris (2018). Roads and Rural Development in Sub-Saharan Africa. https://doi.org/10.1596/29662 [Link]Johary, Rosa; Révillion, Christophe; Catry, Thibault; Alexandre, Cyprien; Mouquet, Pascal; Rakotoniaina, Solofoarisoa; Pennober, Gwenaëlle; Rakondraompiana, Solofo (2023). Detection of Large-Scale Floods Using Google Earth Engine and Google Colab. https://doi.org/10.20944/preprints202309.1375.v1 [Link]Phillip M. Grice; Andy Lee; Henry Ridgely Evans; Charles C. Kemp (2012). The wouse: A wearable wince detector to stop assistive robots, *2*, 165-172. https://doi.org/10.1109/roman.2012.6343748 [Link]Drusch, M.; Del Bello, U.; Carlier, S.; Colin, O.; Fernandez, V.; Gascon, F.; Hoersch, B.; Isola, C.; Laberinti, P.; Martimort, P.; Meygret, A.; Spoto, F.; Sy, O.; Marchese, F.; Bargellini, P. (2012). Sentinel-2: ESA's Optical High-Resolution Mission for GMES Operational Services.

***Remote Sensing of Environment*, *120*, 25-36. https://doi.org/10.1016/j.rse.2011.11.026 [Link]Torres, Ramon; Snoeij, Paul; Geudtner, Dirk; Bibby, David; Davidson, Malcolm; Attema, Evert; Potin, Pierre; Rommen, BjÖrn; Floury, Nicolas; Brown, Mike; Traver, Ignacio Navas; Deghaye, Patrick; Duesmann, Berthyl; Rosich, Betlem; Miranda, Nuno; Bruno, Claudio; L'Abbate, Michelangelo; Croci, Renato; Pietropaolo, Andrea; Huchler, Markus; Rostan, Friedhelm (2012). GMES Sentinel-1 mission. *Remote Sensing of Environment*, *120*, 9-24. https://doi.org/10.1016/j.rse.2011.05.028 [Link]Paul T. Tueller (1989). Remote Sensing Technology for Rangeland Management Applications. *Journal of Range Management*, *42*(6), 442-442. https://doi.org/10.2307/3899227 [Link]Boccia, Valentina; Iannone, Rosario Q.; Gascon, Ferran (2021). Copernicus Sentinel-2 Data From A Card4L Perspective: Preliminary Self-Assessment Performed by Esa. *2021 IEEE International Geoscience and Remote Sensing Symposium IGARSS*, 1994-1996. https://doi.org/10.1109/igarss47720.2021.9554913 [Link]Zhou, Tianjun (2021). New physical science behind climate change: What does IPCC AR6 tell us?. *The Innovation*, *2*(4), 100173. https://doi.org/10.1016/j.xinn.2021.100173 [Link]Wong, Xaria; Toma, Iulia Andreea (2022). Gender and Protection Analysis: Juba, Rumbek and Pibor, South Sudan. https://doi.org/10.21201/2022.8946 [Link]Unknown Author (2022). South Sudan Economic Monitor, February 2022. https://doi.org/10.1596/36994 [Link]Rogan, John; Chen, DongMei (2004). Remote sensing technology for mapping and monitoring land-cover and land-use change. *Progress in Planning*, *61*(4), 301-325. https://doi.org/10.1016/s0305-9006(03)00066-7 [Link]Nyagah, Anthony Mugendi; Mwea, Sixtus Kinyua; Gichaga, Francis John (2021). The Mechanical and Binding Potentials of Fresh Cow Dung (FCD) for Gravel Roads Construction. *East African Journal of Engineering*, *3*(1), 22-32. https://doi.org/10.37284/eaje.3.1.350 [Link]Kristin J. Marks; Michael Whitaker; Nickolas T. Agathis; Onika Anglin; Jennifer Milucky; Kadam Patel; Huong Pham; Pam Daily Kirley; Breanna Kawasaki; James Meek; Evan J. Anderson; Andy Weigel; Sue Kim; Ruth Lynfield; Susan L. Ropp; Nancy Spina; Nancy M. Bennett; Eli Shiltz; Melissa Sutton; H. Keipp Talbot; Andrea Price; Christopher A. Taylor; Fiona P. Havers; COVID-NET Surveillance Team; COVID-NET Surveillance Team; Jeremy Roland; Jordan Surgnier; Carol A. Lyons; Kyle P. Openo; Kenzie Teno; Alexander Kohrman; Erica Bye; Cory Cline; Alison Muse; Virginia Cafferky; Laurie M. Billing; Nasreen Abdullah; William Schaffner; Keegan McCaffrey (2022). Hospitalization of Infants and Children Aged 0–4 Years with Laboratory-Confirmed COVID-19 — COVID-NET, 14 States, March 2020–February 2022. *MMWR Morbidity and Mortality Weekly Report*, *71*(11), 429-436. https://doi.org/10.15585/mmwr.mm7111e2 [Link]**

ReferencesMermiri, M; Bareka, M; Ntalouka, M; Rarras, C; Petsiti, A; Charalabidou, A; Arnaoutoglou, E (2022). B221 Ultrasound guided greater auricular nerve block for red ear syndrome: a case report. *Case report*, A190.1-A190. https://doi.org/10.1136/rapm-2022-esra.295 [Link]Valenzuela, Matías A.; Hernandez, Francisco (2022). Design methodology for Roads Bridges located on Chilean copper miner roads. *IABSE Reports*, *118*, 1789-1795. https://doi.org/10.2749/prague.2022.1789 [Link]Smart, P.L. (1996). Book reviews : Leibundgut, C., editor, 1995: Tracer technologies for hydrological systems. IAHS Publication No. 229. Wallingford: IAHS Press. x + 326 pp. £60.00 paper. ISSN: 0144 7815. *Progress in Physical Geography: Earth and Environment*, *20*(3), 365-366. https://doi.org/10.1177/030913339602000312 [Link]Guha, Shajib; Hossain, Kamal (2022). An economic approach to road condition assessment using road user feedback: A new model and its application. *International Journal of Pavement Engineering*, *24*(2). https://doi.org/10.1080/10298436.2021.2022673 [Link]Raleigh, Clionadh; Linke, Andrew; Hegre, Håvard; Karlsen, Joakim (2010). Introducing ACLED: An Armed Conflict Location and Event Dataset. *Journal of Peace Research*, *47*(5), 651-660. https://doi.org/10.1177/0022343310378914 [Link]Cloude, S.R.; Pottier, E. (1996). A review of target decomposition theorems in radar polarimetry. *IEEE Transactions on Geoscience and Remote Sensing*, *34*(2), 498-518. https://doi.org/10.1109/36.485127 [Link]Ayala, C.; Aranda, C.; Galar, M. (2021). TOWARDS FINE-GRAINED ROAD MAPS EXTRACTION USING SENTINEL-2 IMAGERY. *ISPRS Annals of the Photogrammetry, Remote Sensing and Spatial Information Sciences*, *V-3-2021*, 9-14. https://doi.org/10.5194/isprs-annals-v-3-2021-9-2021 [Link]Workman, Robin; Wong, Patrick; Wright, Alex; Wang, Zhao (2023). Prediction of Unpaved Road Conditions Using High-Resolution Optical Satellite Imagery and Machine Learning. *Remote Sensing*, *15*(16), 3985. https://doi.org/10.3390/rs15163985 [Link]Mushtaq, Fayma; lala, mili; Mantoo, Afaan Gulzar (2021). Trophic state assessment of a freshwater Himalayan lake using Landsat 8 OLI satellite imagery: A case study of Wular Lake. https://doi.org/10.1002/essoar.10505921.2 [Link]Baoyun, Zhao; Yongfei, Li; Wei, Huang; Liyun, Zhang; Wangcheng, Li; Li, Zhang (2021). Mechanical Characteristics of Red Sandstone Under Cyclic Wetting and Drying. https://doi.org/10.21203/rs.3.rs-661816/v1 [Link]Segon, Fabien; Dupuis, Aurélien (2023). AIRBUS DS' HCA: HIGH CAPACITY ACTUATOR FOR SMALL SATELLITE MISSIONS. *Papers of ESA GNC-ICATT 2023*. https://doi.org/10.5270/esa-gnc-icatt-2023-128 [Link]Unknown Author (2023). ESA – European Space Agency. *Encyclopedia of Astrobiology*, 919-919. https://doi.org/10.1007/978-3-662-65093-6_300423 [Link]Ipke Wachsmuth (2002). Max, unser Agent in der virtuellen Welt. *Medical & Biological Engineering & Computing*, *53*(9), 911-20. https://doi.org/10.1007/s11517-015-1299-2 [Link]C. Hersbach et al., "ERA5 hourly data on single levels from (1940). to present," Copernicus Climate Change Service (C3S) CDS, 2023..Al-Hassan, L.A.J.; Al-Abood, A.Y.; Al-Seyab, A.A. (1990). Seasonal variations in the haemoglobin concentration and haematocrit values of Silurus triostegus. *Acta Ichthyologica et Piscatoria*, *20*(1), 99-103. https://doi.org/10.3750/aip1990.20.1.08 [Link]Tan, Brandon Joel (2021). The minimum wage and firm networks: Evidence from South Africa. *WIDER Working Paper*. https://doi.org/10.35188/unu-wider/2021/040-5 [Link]Cigna, Francesca; Jordan, Hannah; Bateson, Luke; McCormack, Harry; Roberts, Claire (2014). Natural and Anthropogenic Geohazards in Greater London Observed from Geological and ERS-1/2 and ENVISAT Persistent Scatterers Ground Motion Data: Results from the EC FP7-SPACE PanGeo Project. *Pure and Applied Geophysics*, *172*(11), 2965-2995. https://doi.org/10.1007/s00024-014-0927-3 [Link]Berg, Claudia N.; Blankespoor, Brian; Selod, Harris (2018). Roads and Rural Development in Sub-Saharan Africa. https://doi.org/10.1596/29662 [Link]Johary, Rosa; Révillion, Christophe; Catry, Thibault; Alexandre, Cyprien; Mouquet, Pascal; Rakotoniaina, Solofoarisoa; Pennober, Gwenaëlle; Rakondraompiana, Solofo (2023). Detection of Large-Scale Floods Using Google Earth Engine and Google Colab. https://doi.org/10.20944/preprints202309.1375.v1 [Link]Phillip M. Grice; Andy Lee; Henry Ridgely Evans; Charles C. Kemp (2012). The wouse: A wearable wince detector to stop assistive robots, *2*, 165-172. https://doi.org/10.1109/roman.2012.6343748 [Link]Drusch, M.; Del Bello, U.; Carlier, S.; Colin, O.; Fernandez, V.; Gascon, F.; Hoersch, B.; Isola, C.; Laberinti, P.; Martimort, P.; Meygret, A.; Spoto, F.; Sy, O.; Marchese, F.; Bargellini, P. (2012). Sentinel-2: ESA's Optical High-Resolution Mission for GMES Operational Services.

***Remote Sensing of Environment*, *120*, 25-36. https://doi.org/10.1016/j.rse.2011.11.026 [Link]Torres, Ramon; Snoeij, Paul; Geudtner, Dirk; Bibby, David; Davidson, Malcolm; Attema, Evert; Potin, Pierre; Rommen, BjÖrn; Floury, Nicolas; Brown, Mike; Traver, Ignacio Navas; Deghaye, Patrick; Duesmann, Berthyl; Rosich, Betlem; Miranda, Nuno; Bruno, Claudio; L'Abbate, Michelangelo; Croci, Renato; Pietropaolo, Andrea; Huchler, Markus; Rostan, Friedhelm (2012). GMES Sentinel-1 mission. *Remote Sensing of Environment*, *120*, 9-24. https://doi.org/10.1016/j.rse.2011.05.028 [Link]Paul T. Tueller (1989). Remote Sensing Technology for Rangeland Management Applications. *Journal of Range Management*, *42*(6), 442-442. https://doi.org/10.2307/3899227 [Link]Boccia, Valentina; Iannone, Rosario Q.; Gascon, Ferran (2021). Copernicus Sentinel-2 Data From A Card4L Perspective: Preliminary Self-Assessment Performed by Esa. *2021 IEEE International Geoscience and Remote Sensing Symposium IGARSS*, 1994-1996. https://doi.org/10.1109/igarss47720.2021.9554913 [Link]Zhou, Tianjun (2021). New physical science behind climate change: What does IPCC AR6 tell us?. *The Innovation*, *2*(4), 100173. https://doi.org/10.1016/j.xinn.2021.100173 [Link]Wong, Xaria; Toma, Iulia Andreea (2022). Gender and Protection Analysis: Juba, Rumbek and Pibor, South Sudan. https://doi.org/10.21201/2022.8946 [Link]Unknown Author (2022). South Sudan Economic Monitor, February 2022. https://doi.org/10.1596/36994 [Link]Rogan, John; Chen, DongMei (2004). Remote sensing technology for mapping and monitoring land-cover and land-use change. *Progress in Planning*, *61*(4), 301-325. https://doi.org/10.1016/s0305-9006(03)00066-7 [Link]Nyagah, Anthony Mugendi; Mwea, Sixtus Kinyua; Gichaga, Francis John (2021). The Mechanical and Binding Potentials of Fresh Cow Dung (FCD) for Gravel Roads Construction. *East African Journal of Engineering*, *3*(1), 22-32. https://doi.org/10.37284/eaje.3.1.350 [Link]Kristin J. Marks; Michael Whitaker; Nickolas T. Agathis; Onika Anglin; Jennifer Milucky; Kadam Patel; Huong Pham; Pam Daily Kirley; Breanna Kawasaki; James Meek; Evan J. Anderson; Andy Weigel; Sue Kim; Ruth Lynfield; Susan L. Ropp; Nancy Spina; Nancy M. Bennett; Eli Shiltz; Melissa Sutton; H. Keipp Talbot; Andrea Price; Christopher A. Taylor; Fiona P. Havers; COVID-NET Surveillance Team; COVID-NET Surveillance Team; Jeremy Roland; Jordan Surgnier; Carol A. Lyons; Kyle P. Openo; Kenzie Teno; Alexander Kohrman; Erica Bye; Cory Cline; Alison Muse; Virginia Cafferky; Laurie M. Billing; Nasreen Abdullah; William Schaffner; Keegan McCaffrey (2022). Hospitalization of Infants and Children Aged 0–4 Years with Laboratory-Confirmed COVID-19 — COVID-NET, 14 States, March 2020–February 2022. *MMWR Morbidity and Mortality Weekly Report*, *71*(11), 429-436. https://doi.org/10.15585/mmwr.mm7111e2 [Link]**